Since January 2020 Elsevier has created a COVID-19 resource centre with free information in English and Mandarin on the novel coronavirus COVID-19. The COVID-19 resource centre is hosted on Elsevier Connect, the company's public news and information website.

Biosensors and Bioelectronics 228 (2023) 115202

Contents lists available at ScienceDirect

Biosensors and Bioelectronics

journal homepage: www.elsevier.com/locate/bios

Ultra-sensitive label-free SERS biosensor with high-throughput screened DNA aptamer for universal detection of SARS-CoV-2 variants from clinical samples

Ki Sung Park [a], Anna Choi [a], Hyun Jung Kim [a,b], Insu Park [a,c], Mi-Suk Eom [d], Sang-Gu Yeo [d], Ryeo Gang Son [a], Tae-In Park [a], Gyudo Lee [a], Hyongsok Tom Soh [e,f], Yoochan Hong [b,**], Seung Pil Pack [a,*]

[a] Department of Biotechnology and Bioinformatics, Korea University, Sejong, 30019, Republic of Korea
[b] Department of Medical Device, Korea Institute of Machinery and Materials (KIMM), Daegu, 42994, Republic of Korea
[c] Department of Biomedical Engineering, Konyang University, Daejeon, 35365, Republic of Korea
[d] Division of Infectious Diseases, Sejong Institute of Health & Environment, Sejong, 30015, Republic of Korea
[e] Department of Electrical Engineering, Stanford University, Stanford, CA, 94305, USA
[f] Department of Radiology, Stanford University, Stanford, CA, 94305, USA

ARTICLE INFO

Keywords:
SARS-CoV-2 spike binding aptamer
Particle display
Silver nanoforest
SERS-based aptasensor
Label-free SERS biosensor

ABSTRACT

COVID-19, severe acute respiratory syndrome coronavirus 2 (SARS-CoV-2), has caused an ongoing global pandemic with economic and social disruption. Moreover, the virus has persistently and rapidly evolved into novel lineages with mutations. The most effective strategy to control the pandemic is suppressing virus spread through early detection of infections. Therefore, developing a rapid, accurate, easy-to-use diagnostic platform against SARS-CoV-2 variants of concern remains necessary. Here, we developed an ultra-sensitive label-free surface-enhanced Raman scattering-based aptasensor as a countermeasure for the universal detection of SARS-CoV-2 variants of concern. In this aptasensor platform, we discovered two DNA aptamers that enable binding to SARS-CoV-2 spike protein via the Particle Display, a high-throughput screening approach. These showed high affinity that exhibited dissociation constants of 1.47 ± 0.30 nM and 1.81 ± 0.39 nM. We designed a combination with the aptamers and silver nanoforest for developing an ultra-sensitive SERS platform and achieved an atto-molar (10^{-18} M) level detection limit with a recombinant trimeric spike protein. Furthermore, using the intrinsic properties of the aptamer signal, we demonstrated a label-free aptasensor approach, enabling use without the Raman tag. Finally, our label-free SERS-combined aptasensor succeeded in detecting SARS-CoV-2 with excellent accuracy, even in clinical samples with variants of concern, including the wild-type, delta, and omicron variants.

1. Introduction

Severe acute respiratory syndrome coronavirus 2 (SARS-CoV-2), the pathogen responsible for COVID-19 (Wu et al., 2020), has caused an ongoing global pandemic with high morbidity and mortality, severely threatening public health and the global economy (Podder et al., 2021; Yang et al., 2021). Effective control of pandemics like COVID-19 should focus on the early detection of infections (Spinelli and Pellino, 2020). Vaccines from Moderna, Pfizer-BioNTech, Johnson & Johnson, Novavax and others are now widely available (Banerji et al., 2021), but early diagnosis of SARS-CoV-2 continues to play an essential role in reducing virus spread. Further development of advanced rapid diagnostic tools will be valuable both here and as a countermeasure for preventing and controlling future pandemics (Simpson et al., 2020).

Currently, early detection of SARS-CoV-2 is primarily achieved by reverse transcription-quantitative polymerase chain reaction (RT-qPCR)-based molecular diagnostics (Emery et al., 2004; Corman et al., 2020). However, these assays entail a turnaround time of >24 h to screen and diagnose patients with suspected SARS-CoV-2 infection. Lateral-flow-based immunoassays (Li et al., 2020) and CRISPR-based

* Corresponding author.
** Corresponding author.
E-mail addresses: ychong1983@kimm.re.kr (Y. Hong), spack@korea.ac.kr (S.P. Pack).

https://doi.org/10.1016/j.bios.2023.115202
Received 5 December 2022; Received in revised form 28 February 2023; Accepted 4 March 2023
Available online 8 March 2023

tests (e.g., SHERLOCK (Kellner et al., 2019) and DETECTR (Broughton et al., 2020)) can shorten the time required for diagnosis, but typically require high production costs owing to their reliance on antibodies or enzymes. Rapid antigen tests (RATs) such as the lateral-flow immunoassay can be effective for generating quick results at the point of care, but also face hurdles including a high false-positive rate (Gans et al., 2022). As such, there remains an unmet need for rapid, low-cost diagnostics that can achieve high sensitivity and selectivity for target analytes.

Aptamers are single-stranded DNA or RNA reagents with high affinity and specificity to specific target molecules (Ellington and Szostak, 1990). Compared with monoclonal antibodies, DNA aptamers have several benefits, including thermal and pH stability, small size, and straightforward chemical synthesis (Jayasena, 1999), which means that they can be easily and reproducibly produced and modified at a low cost (Zhou and Rossi, 2017). Several DNA aptamer-based analytical approaches have already been developed, such as the aptamer-based lateral-flow assay (Chen and Yang, 2015), the enzyme-linked oligonucleotide assay (ELONA) (Drolet et al., 1996), and aptamer-based field effect transistor (FET) biosensors (Park et al., 2021; Hwang et al., 2021). However, although ultra-sensitive detection methods have been achieved by incorporating aptamers into various sensing platforms (Hu et al., 2012; Taghdisi et al., 2016), these typically require aptamer modification with labels for signal reporting at the 5′ or 3′ end of the aptamer sequence, which increases the production cost in terms of chemical synthesis.

As an alternative, we have developed a label-free surface-enhanced Raman scattering (SERS)-based aptamer sensor. In the last decade, SERS-based aptasensors have been intensively explored for sensitive detection of analytes ranging in size from small-molecule targets to protein targets (Scatena et al., 2019). Although Raman scattering is not inherently ideal for biological applications owing to its inherently weak signal, the use of SERS can provide up to 10^8-fold signal enhancement. This enhancement is derived from the molecular vibrations of analyte molecules on the surface of a nanostructured metal substrate, coupled with locally-amplified electromagnetic fields (Moskovits, 1985; Ambartsumyan et al., 2020). In this study, we isolated two novel DNA aptamers against SARS-CoV-2 spike (S) protein through four rounds of screening using particle display (Wang et al., 2014), a powerful high-throughput aptamer screening approach. The S protein is located on the SARS-CoV-2 surface and is the primary antigen employed in COVID-19 diagnostic tests, allowing aptamer access to the virus surface and rapid detection without virus lysis. Two aptamers were conjugated on a silver nanoforest (SNF) substrate, which was fabricated with a three-dimensional nanostructure in order to achieve effective enhancement of Raman signals using an intrinsic property of the aptamer (Fig. 1). Using this label-free aptasensor approach, we were able to achieve ultra-sensitive detection of the recombinant trimeric S protein, with a detection limit of 100 fg/mL (240 aM). We were able to further validate this assay's diagnosis performance with excellent accuracy in clinical samples, for both the wild-type Wuhan strain as well as the newer delta and omicron variants.

2. Materials and methods

2.1. Materials and reagents

Rhodamine 6G, tris(2-carboxyethyl)phosphine hydrochloride (TCEP), sorbitan monooleate (Span-80), polysorbate-80 (Tween-80), Triton X-100, and mineral oil were purchased from Sigma-Aldrich (St Louis, MO, USA). Carboxylic acid-functionalized MyOne magnetic particles (1 μm size) were purchased from Invitrogen. Dulbecco's phosphate-buffered saline (DPBS) was purchased from Biowest (Nuaillé, France). Silver was purchased from iNexus Inc. (Seongnam, Korea). GoTaq PCR master mix, GoTaq polymerase, and dNTPs were purchased from Promega Corporation (Madison, WI, USA). Recombinant SARS-CoV-2 spike (S) protein extracellular domain (ECD) (ref 40589-V08H4), subunit 1 (ref 40591-V08H), subunit 2 (ref 40590-V08H1),

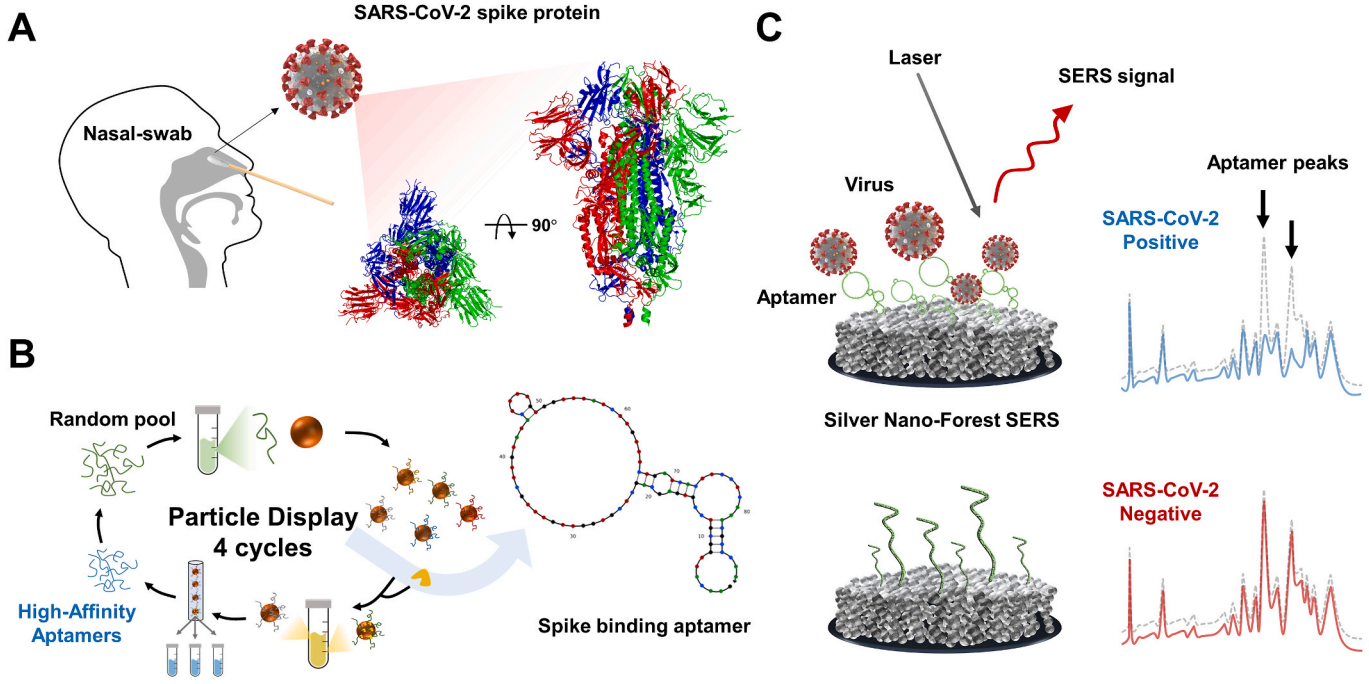

Fig. 1. Design strategy for our label-free SERS-based aptasensor platform for SARS-CoV-2. (A) Targeted aptamer screening against spike (S) protein for detecting SARS-CoV-2 from clinical samples. Side and top view of the trimeric S protein on the surface of SARS-CoV-2 (PDB: 6VXX). (B) The particle display aptamer discovery process, in which solution-phase aptamer library molecules are converted to monoclonal aptamer particles, incubated with fluorescently-labeled S protein, and then subjected to fluorescence-activated cell sorting (FACS) to enrich library molecules with strong affinity for this target. (C) The aptamer is then conjugated onto a silver nanoforest (SNF) substrate for the detection of SARS-CoV-2. The intrinsic aptamer peaks shift in response to the conformational changes triggered by S protein binding to the aptamer.

and receptor binding domain (RBD) (ref 40592-V08H) were purchased from Sino Biological (Beijing, China).

2.2. Library and primer construction

The single-stranded DNA (ssDNA) library, modified aptamer, and primers were synthesized by Integrated DNA Technologies (IDT; Coralville, IA, USA). The 90-mer Shao library (Shao et al., 2011) comprised 52-nt randomized sequences flanked by 19-nt PCR primer sites: 5′-GAACATTGGCGTCCGTGAG-[N52]-CACTTCCTCAAACGCCCAA-3′. The randomized sequences were synthesized with an equal probability of A, T, G, or C. All sequences described in this work are listed in Table S1.

2.3. Forward primer (FP) conjugation to magnetic particles

Carboxylic acid-functionalized MyOne magnetic particles (1 μm size, 500 μL with 10^7/μL) were washed using 500 μL of 0.01 N sodium hydroxide (NaOH) and washed thrice with an equal volume of ultra-pure water. After washing, the beads were re-suspended in a 150 μL reaction mixture containing 30 nmol of 5′-C12-amino-modified FP, 250 mM 1-ethyl-3-(3-dimethylaminopropyl)carbodiimide (EDC), 1 mM imidazole chloride, and 200 mM NaCl. The mixture was vortexed and sonicated, and then incubated for 16 h at 25°C with gentle rotation. After complete covalent coupling, the remaining functional groups on the particle surfaces were blocked with 20 mM amino-PEG-methyl. Finally, the FP-coated beads were washed twice with quenching buffer (50 mM Tris-HCl buffer, pH 8.0, with 0.05% Tween-20) and stored in 500 μL of 0.01% Tween-20 in 10 mM Tris-HCl buffer, pH 8.0. To characterize the FP conjugation efficiency, the FP-coated beads were hybridized with 1 μM FAM-modified FP-complementary oligonucleotides in PBST (0.025% Tween-20 in DPBS) buffer, followed by fluorescence analysis using flow cytometry (Fig. S1).

2.4. Aptamer particle generation using emulsion PCR (ePCR)

The oil phase comprised 0.05% Triton X-100, 0.45% Tween-80, and 4.5% Span-80 in mineral oil. The aqueous phase comprised 1x PCR master mix, 40 nM FP, 1 μM reverse primer (RP), 62.5 U/mL GoTaq polymerase, 3.5 mM of each dNTP, 25 mM $MgCl_2$, 3 pM library pool, and 3×10^8 FP-coated beads in a final volume of 1 mL. The emulsion was generated using an Ultra-Turrax Device (IKA) with a DT-20 tube (IKA) at 500 rpm for 5 min. The ePCR was carried out as the following cycling conditions: 95°C for 3 min, followed by 50 cycles of 95°C for 30 s, 58°C for 30 s, and 72°C for 75 s. Then, the emulsion was broken, and the aptamer particles were cleaned up. Based on the Poisson distribution, we estimated that 20 ± 15% of the synthesized aptamer particles should include beads displaying the PCR product, favoring the generation of monoclonal aptamer particles (Dressman et al., 2003; Diehl et al., 2006; Wang et al., 2014). To characterize these particles, the synthesized beads were hybridized with 1 μM FAM-modified reverse primer in PBST buffer, followed by fluorescence analysis using flow cytometry (Fig. S2).

2.5. Preparation of monoclonal aptamer particles

After cloning and sequencing, the monoclonal aptamer particles displaying individual aptamer sequences were generated by particle PCR. Each 100 μL particle PCR comprised 1 × PCR Master Mix, 25 mM $MgCl_2$, 1 μM FAM-modified RP, 10 nM aptamer template, and 3×10^7 FP-coated particles. PCR was carried out under the following conditions: 95°C for 3 min, followed by 25 cycles of 95°C for 30 s, 58°C for 30 s, and 72°C for 45 s. To avoid particle aggregation and increase particle PCR efficiency, it was vortexed and sonicated the reaction every five cycles at the 72°C elongation step. After PCR amplification, the fluorescence intensities were measured using flow cytometry to confirm the particle PCR efficiency.

2.6. Binding assay and specificity test

The relative binding abilities of aptamer candidates in each consensus sequence were confirmed through a bead-based fluorescence binding assay (Ahmad et al., 2011). Each of the monoclonal aptamer particle preparations was incubated with 100 nM biotinylated S protein trimer, receptor-binding domain (RBD), subunit 1 (S1), subunit 2 (S2) and BSA, respectively, for 1 h in PBSMCT (1 mM $MgCl_2$, 1 mM $CaCl_2$, 0.025% Tween-20 in DPBS) binding buffer. After binding, the particles were washed thrice, followed by labeling with 50 nM Alexa Fluor 647-conjugated streptavidin (Invitrogen, CA, USA) in a binding buffer for 10 min. It is crucial to limit the labeling time to avoid non-specific binding during fluorescence labeling. We then washed the beads thrice with a binding buffer and measured the fluorescence using flow cytometry.

2.7. Measurement of binding affinity

To measure the binding affinities of the consensus sequences, an individual monoclonal aptamer particle was generated by particle PCR following the protocol above. The aptamer displayed particle was incubated with various concentrations of biotinylated S protein (serially diluted from 150 nM to 0.07 nM). All samples were washed thrice and labeled with 50 nM Alexa Fluor 647-conjugated streptavidin under equal conditions. The aptamer-target complex on the bead was washed thrice with binding buffer, and the fluorescence intensities were measured using flow cytometry. The dissociation constant was calculated using GraphPad software with one site–specific binding equation:

$$Y = Bmax \times X / (Kd + X)$$

2.8. Fabrication of the silver nanoforest (SNF) substrate

In previous work, our group established the fabrication of the SNF substrate using the nano-sputtering method (Kim et al., 2021). SERSpace substrates without surface modifications were provided by Kwang-Lim Precise Manufacturing. Briefly, the system conducted for nano-sputtering-based fabrication for nano-structure was applied to fabricate the nano-porous silver structures, and the SNF substrates were fabricated on six-inch silicon wafers. The basic conditions for fabrication of silver nanoporous structured substrate were as follows. The aperture diameter and length of the nano-sputtering system were 5 mm and 45 mm, respectively. The additional conditions were considered to fabricate SNF substrate: 400 mTorr of sputtering pressure in clustering chamber; 300 W of DC power for cluster source; and 20°C of temperature for cluster source. 85 and 15 sccm of the gas flow rates were used for argon and helium, respectively. Additionally, the finished substrate on six-inch wafer was cut to a size of 4×4 mm^2.

2.9. Surface modification of the SNF substrate

To activate the –SH groups at the 5′ end of the aptamers, the aptamers were treated with 100x TCEP for 4 h at 25°C. The remaining reactant was removed by centrifugation using Centricon (Amicon, Beverly, MA, USA) with a 1.5 mL microcentrifuge tube at 13,500 rpm for 30 min. DPBS buffer was added to the samples to adjust the pH to 7. 10 μL of the resulting aptamer solution (1 μM) was then dropped onto the SNF substrate and dried at 25°C for 1 h. The SNF substrates treated with aptamer solution were washed using DPBS for 4 h with gentle stirring and dried at 25°C.

2.10. SERS signal measurements

A 785 nm excitation laser in an upright microscope (Olympus, Japan) was used to acquire SERS signals from samples. It applied 80 mW of laser power, with 1 s of integration time. The Raman signal of the

aptamer was measured at a specific position before sample treatment, and again at the same position after sample treatment, with locations confirmed using a microscope. The sample volume used in this study was fixed at 10 μL. The incubation time between aptasensor and samples was also set for 5 min. All experiments with SERS signal measurements were carried out under identical conditions.

2.11. Clinical samples and RT-qPCR

Nasopharyngeal swab samples from patients were collected in viral transport media (VTM) on different dates. These samples were obtained from the Sejong Institute of Health & Environment. SARS-CoV-2 was determined by RT-qPCR using a Standard M nCoV Real-Time Detection Kit according to the manufacturer's protocol (SD Biosensor, Republic of Korea). SARS-CoV-2 delta (B1.617.2) and omicron (B.1.1.529) variants were detected using a PowerChek SARS-CoV-2 S-gene Mutation Detection Kit (Kogene Biotech, Republic of Korea). The Raman signals from clinical samples were measured under the following conditions. The 10 μL of the sample was incubated with SpS1-C4 aptamer-conjugated silver nanoforest for 5 min, the washing was conducted using DW, and the average spectrum was obtained by measuring ten spectra per sample.

3. Results and discussion

3.1. Particle display selection of novel DNA aptamers against SARS-CoV-2 S protein

The S protein is located on the SARS-CoV-2 surface and facilitates entry into host cells by interacting with human angiotensin-converting enzyme 2 (ACE2), and this protein is the primary antigen employed in COVID-19 diagnostics, as it is accessible on the virus surface and thus allows rapid detection without virus lysis. As the target antigen for aptamer screening in this study, we used the recombinant SARS-CoV-2 S protein extracellular domain (ECD), which is optimized for pre-formation of a homotrimer. Several proline mutations (F817P, A892P, A899P, A942P, K986P, V987P) and alanine mutations (R683A and R685A) were introduced to stabilize the pre-fusion state of the homotrimer and abolished the furin cleavage site, respectively (Hsieh et al., 2020).

To effectively and economically discover high-affinity aptamers, we employed the particle display (Wang et al., 2014) screening platform, which quantitatively measures the binding ability of monoclonal aptamer particles derived from every aptamer candidate in a random pool and then individually sorts them using FACS in a high-throughput manner. In this approach, the aptamer particles are synthesized using an emulsion polymerase chain reaction (ePCR) (Shao et al., 2011). The

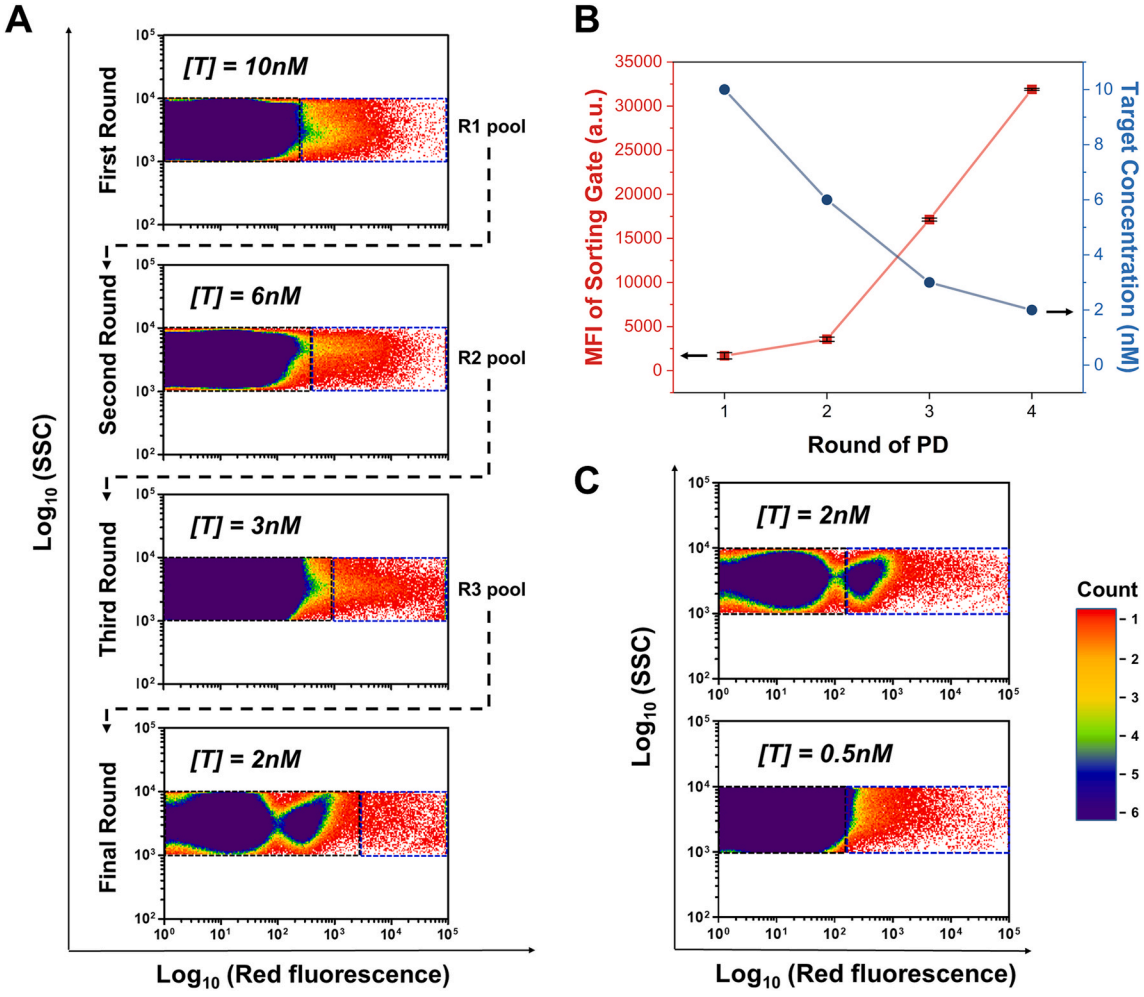

Fig. 2. Round by round assessment of the particle display screening process. (A) FACS dot plots from all four rounds of screening at the stated concentrations (*[T]*) of recombinant trimeric S protein. (B) Mean fluorescence intensity (MFI) within the sort gate at different target concentrations in each of the four rounds. (C) Additional sorting experiments in the final round of screening with another sort gate at different target concentrations. Overall, 5% of the top binders at 2 nM, 0.15% of the top binders at 2 nM, and 0.1% of the top binders at 0.5 nM of S protein were sorted using FACS.

aptamer candidates displayed on the particles are then incubated with fluorescently-labeled target, and the fluorescence intensity of each particle is measured using FACS. These intensities enable quantitative determination of aptamer affinity and the effective separation of weak and strong binders. Finally, the sorted high-affinity aptamer particles are directly amplified by PCR, and this enriched pool of aptamer candidates is used in the next selection round. Prior to particle display screening, we performed two rounds of conventional selection with a pool of 10^{14} randomized library molecules using S protein-immobilized magnetic beads, because the FACS instrument has a practical throughput limitation of 4×10^7 particles per h. We then used this pre-selected pool for particle display screening with an initial library of 10^8 aptamer particles. Four rounds (R1–R4) of screening were performed by reducing the target concentration in a stepwise manner from 10 nM to 2 nM (Fig. 2A). We set the sort gate to collect 0.1–0.2% of the top binder population with the strongest fluorescence signals in the FACS dot plot (Fig. 2A, blue box). As a control, the fluorescence intensity of forward primer (FP)-coated particles with no aptamer expressed was measured in order to calibrate the "reference gate" for non-binders in the FACS screen (Fig. 2A, black box). In R1, to avoid losing high-affinity aptamer candidates, we began selection with a low screening stringency by setting a wide sort gate. The isolated aptamer candidates were then amplified by PCR to synthesize the aptamer particles for the next round. In subsequent rounds, we further narrowed the sort gate thresholds to increase the screening stringency. After R2, the population shift of the red fluorescence signal was greatly increased, indicating that high-affinity aptamer candidates were being enriched (Fig. 2B). By R4, there was no further population shift in terms of fluorescence, and we therefore determined that we had achieved peak enrichment and stopped screening in order to perform sequencing analysis of the enriched pool.

We initially tried to isolate the top binders from R4 based on binding to 2 nM S protein, but this yielded an excessively large population with strong red fluorescence. Unlike in other rounds, there were two large populations represented within the reference gate in the R4 pool, one of which appeared to be budding off from the other (Fig. 2A). To investigate whether the best aptamer sequence belonged to a large population with moderate fluorescence intensities in this 'budding' population or the sort-gated population with the highest fluorescence intensities, we sorted out the different populations at different concentrations (Fig. 2C). The sort gates were set separately into groups of 0.15% top binders and 5% top binders, respectively, of round 4 sorting at 2 nM concentration. In addition, a separate sorting experiment was performed that collected 0.1% of top binders of the same round 4 pool at 0.5 nM as the optimal concentration of S protein based on the result of the extra binding assay.

3.2. Selection of a high-affinity S protein-binding DNA aptamer

We then performed bacterial cloning and Sanger sequencing of R4 sorted DNA aptamer candidates. Our sequencing analysis revealed four different consensus sequences. Two of these, SpS1-C1 and C2, were respectively observed among the 0.15% and 5% top binders from the 2 nM S protein sorting condition, whereas the other two groups (SpS1-C3 and -C4) were only observed in the top binders from the 0.5 nM S protein extra sorting experiment (Table 1). These aptamer candidates were individually synthesized as monoclonal aptamer particles via PCR amplification on forward primer-coated magnetic beads. Next, a binding assay was performed with each monoclonal aptamer particle to find the best S protein aptamer candidate via FACS analysis. The results showed that SpS1-C1 and SpS1-C4 clearly exhibited the greatest target affinity (Fig. 3A). And then, the specificity test was conducted on the receptor-binding domain (RBD), subunit 1 (S1), and subunit 2 (S2) domain of the S protein to confirm the aptamer binding sites, with BSA as a control. These results indicate that both aptamers specifically bind to S1 domain of the S protein (Fig. 3B). Finally, the binding affinity of the two aptamers was determined using fluorescently-labeled S protein trimers through a bead-based fluorescence binding assay (Ahmad et al., 2011). The binding data were evaluated using GraphPad software with a 1:1 binding model to determine the dissociation constant (Kd) values (Fig. 3C and D). The two aptamers exhibited excellent affinity, with Kd values of 1.47 ± 0.30 nM and 1.81 ± 0.39 nM for SpS1-C1 and -C4, respectively.

3.3. A label-free SERS-based DNA aptasensor for ultra-sensitive detection of S protein

We then designed a label-free, SERS-based aptasensor using these newly generated DNA aptamers. To achieve effective enhancement of Raman signals, we fabricated a three-dimensional nanostructured silver nanoforest (SNF) substrate (Kim et al., 2021) using the nano-sputtering method (Fig. 4A), followed by conjugation of the two spike-binding aptamers onto the surface of the SNF substrate. Further, it is widely accepted that silver nanoparticles exhibit higher SERS enhancement than gold nanoparticles (Zhao et al., 2008). We also were able to observe the intrinsic signal of DNA aptamer on the SNF substrate. This intrinsic signal-based aptasensor enables detection without the need for incorporation of any Raman labels.

First, the morphology of the SNF substrate was verified via scanning electron microscopic (SEM) analysis (Fig. 4B). This revealed a silver nanoporous structure with a thickness of approximately 1.2 μm; for reference, the original silver nanoparticles were approximately 75 nm in diameter. This three-dimensional nanostructure should be capable of effectively amplifying Raman signals. To verify the suitability of the SNF substrate, the SERS signals were measured, which were produced by droplets of a solution containing various concentrations of rhodamine 6G (R6G) solution, a well-known Raman tag (Fig. 4C). We confirmed the presence of the R6G-specific peak at 1,511 cm^{-1}, which is the product of aromatic C–C stretching vibrations (Pang et al., 2014). We subsequently plotted the Raman intensity at 1,511 cm^{-1} relative to the concentration of R6G, and confirmed that as the R6G concentration decreased, the magnitude of this peak also decreased (Fig. 4D). Based on this analysis, we determined a detection limit of 2×10^{-12} mol. In order to confirm the usability of the SNF substrate as a SERS substrate, the reproducibility

Table 1
Consensus sequences from the R4 aptamer pool.

Aptamer ID	Sequence (5′–3′)	Length	Sorting Condition
SpS1-C1	GAACATTGGCGTCCGTGAG-TGAGACCATAGTCCAGCGAACTAAACCTACCCTAAAGGGCAAGGAAGACGGG-CACTTCCTCAAACGCCCAA	90mer	0.15%@2 nM
SpS1-C2	GAACATTGGCGTCCGTGAG-CTGCAATATCTTCTTCAATGCCCTGCTGCCACCACTGGCTTCACTTGCGTGT-CACTTCCTCAAACGCCCAA	90mer	5.0%@2 nM
SpS1-C3	GAACATTGGCGTCCGTGAG-AGATTATAATCCATCTGACGAGTTGTTTTACCGATATTTATCAGTTTTTGTT-CACTTCCTCAAACGCCCAA	90mer	0.1%@0.5 nM
SpS1-C4	GAACATTGGCGTCCGTGAG-CAGCTCGTGGTTGTTTGCTTGTATACTTTTGTGGTTTATCTTGTTTCTGAT-CACTTCCTCAAACGCCCAA	89mer	0.1%@0.5 nM

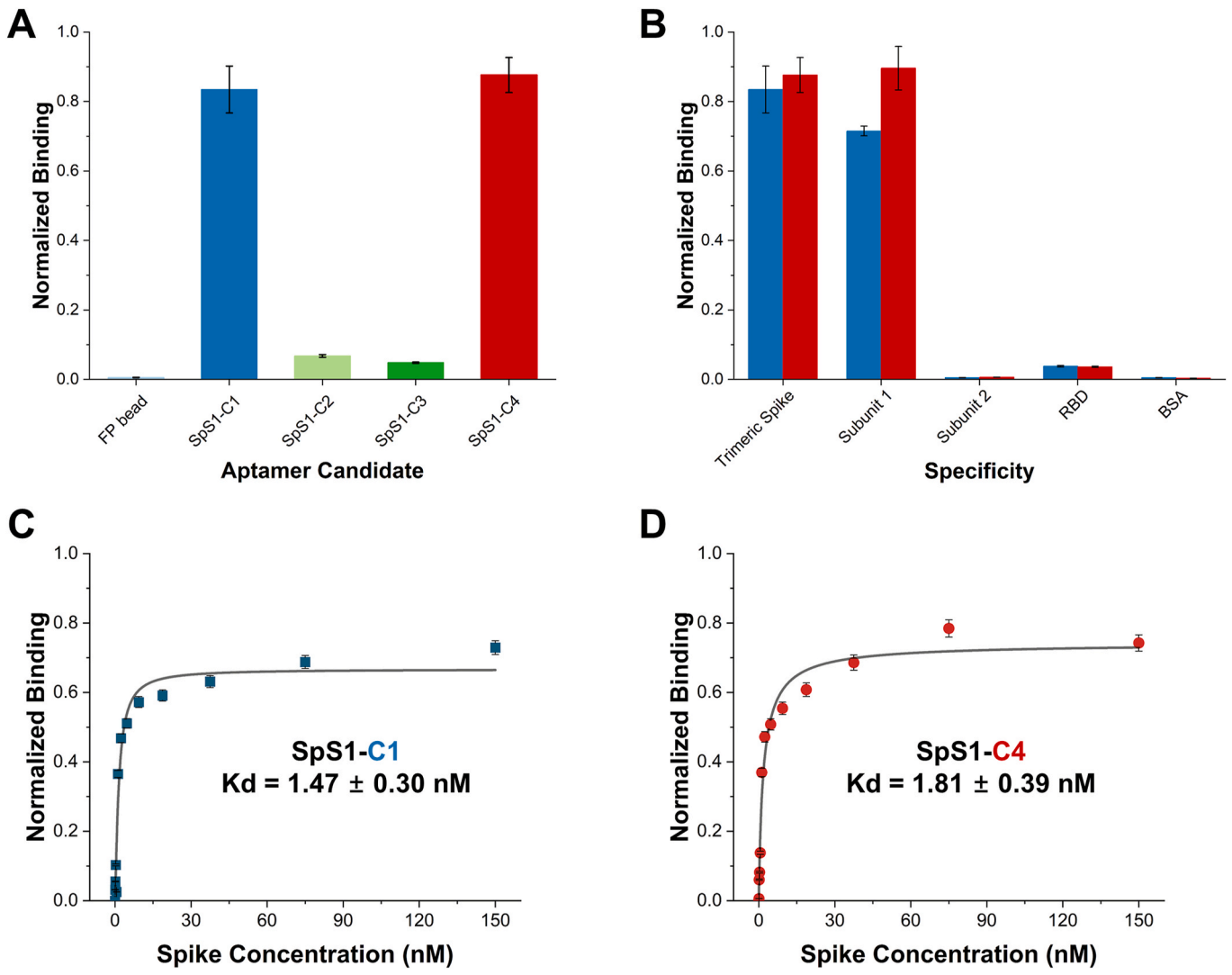

Fig. 3. Characterization of the isolated S protein-binding aptamers. (A) Candidate aptamers from each of the four consensus sequence families were chosen for further analysis. 'FP bead' indicates the forward primer-coated bead used as a negative control. (B) Specificity measurements were also conducted against the trimeric S protein, subunit 1, subunit 2, the receptor-binding domain (RBD), and bovine serum albumin (BSA). (C, D) Dissociation constant (Kd) measurements of the best aptamers using a bead-based fluorescence assay. Kd was calculated from the fluorescence intensity of binding in a 1:1 binding model using GraphPad software.

and anti-interference capability of the SNF substrate were confirmed (Fig. S4 and Fig. S5). The reproducibility of SNF substrate was analyzed through Raman signal measurement of R6G with a concentration of 1 mM for 20 different SNF substrates, and the error range was about 6.67%. In addition, the anti-interference capability of the SNF substrate was confirmed using a mixture of R6G and Nile blue A, and it was confirmed that the characteristic peak (599 cm^{-1}) of Nile Blue A was well measured in this mixture. Furthermore, Fourier transform infra-red (FTIR) analysis was also conducted (Fig. S6). It was observed that no peak occurred on the bare SNF substrate. In comparison, the aptamer-conjugated SNF showed that two peaks of 1,429 cm^{-1} and 2, 962 cm^{-1} caused by O–H bending of carboxyl acid and C–H stretching of alkanes, respectively. In addition, X-ray diffraction (XRD) patterns were also analyzed for bare SNF substrate and aptamer conjugated SNF substrate (Fig. S7). XRD peaks at 2θ of 38.18°, 44.25°, 64.72°, and 77.40° could be attributed to the (111), (200), (220), and (311) crystallographic planes of the face-centered cubic silver crystals, respectively. Therefore, the XRD pattern clearly demonstrated that Ag-based nanostructures were formed in this research. The main crystalline phase was silver, and there were no obvious other phases, such as impurities, found in the XRD patterns. Finally, the long-term stability of aptasensor over 5 days was also confirmed (Fig. S8). The intensities at 1,587 cm^{-1} were barely changed. From these results, we were able to successfully form a nanoscale gap, and using this, we manufactured an SNF substrate, which was confirmed to be available as a SERS substrate. The nanoscale gap used here formed a strong hot spot by forming a three-dimensional nanoporous structure, which is thought to have amplified the Raman signal of the sample.

We then conjugated SpS1-C1 and -C4 aptamers onto the surface of the SNF substrate. These aptamers were modified with a thiol group at the 5′-end to ensure consistent orientation after immobilization, which could in turn enhance binding affinity (Abdelhamid et al., 2022). We first recorded the intrinsic Raman signals of the conjugated aptamers on the SNF surface (Fig. 4E–G). We observed a strong Raman signal in the 1, 400–1,600 cm^{-1} spectral range, corresponding to the vibrations of ketones and some guanine deformation (Gillibert et al., 2018). We also saw several additional peaks, including a 768 cm^{-1} peak corresponding to the C–C and C–N stretching of adenine and thymine (Barhoumi and Halas, 2010) and a 1,317 cm^{-1} peak produced by the N–C of adenine and guanine (Gao et al., 2017) (Fig. S9). Next, we added the recombinant trimeric S protein to the aptamer-conjugated SNF substrate at varying concentrations. The Raman signals of the two aptamers were

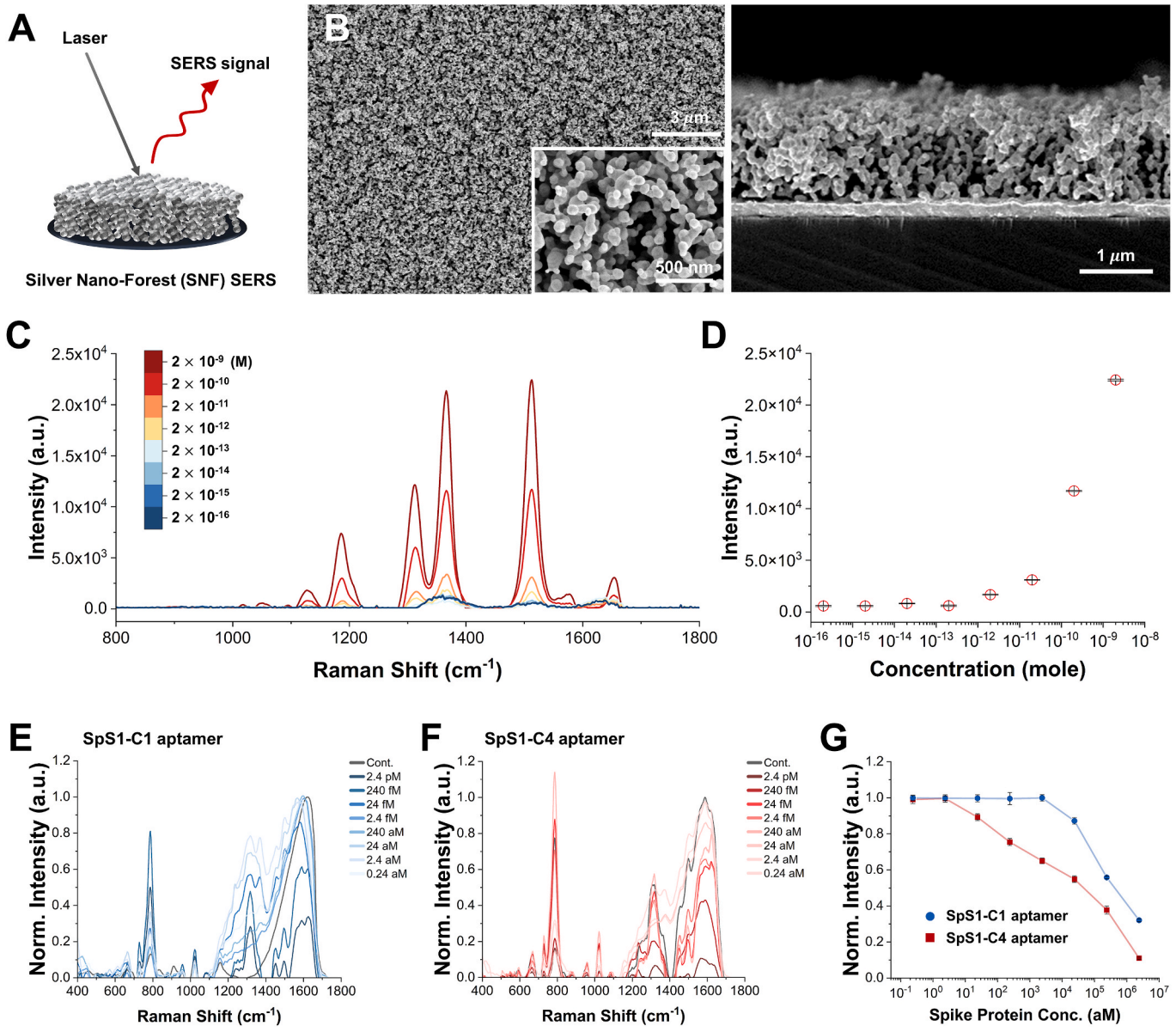

Fig. 4. Design of the label-free SERS-based aptasensor. (A) Schematic illustration of SERS analysis using the SNF substrate. (B) Top and side view scanning electron microscopy (SEM) images of the SNF substrate. (C) Raman spectra with varying concentrations of rhodamine 6G on the SNF substrate. (D) Concentration-dependent Raman intensity of rhodamine 6G at 1,511 cm^{-1}. (E–G) Raman shifts of intrinsic signals for (E) SpS1-C1 and (F) SpS1-C4 at varying concentrations of the recombinant trimeric S protein. (G) The data show the detection limit of SpS1-C1 and -C4 on the SNF substrate based on Raman signal intensity at 1,587 cm^{-1}.

considerably altered at the highest concentration of S protein (10 ng/mL), and as the protein concentration decreased, the Raman signal changes also decreased. At low concentrations such as 1 or 10 pg/mL, the Raman signal was virtually unchanged relative to before protein administration. To further quantify this concentration-dependent response, we focused specifically on the above-mentioned peaks in Raman intensity at positions 768, 1,317, and 1,587 cm^{-1}. We chose the Raman signal at 1,587 cm^{-1} with the most prominent signals and the smallest experimental error compared to the other two positions (768 and 1,317 cm^{-1}) (Fig. 4E–G and Fig. S9). We confirmed a detection limit of 240 fM and 240 aM for aptamers SpS1-C1 and -C4, respectively, using 1,587 cm^{-1} Raman signals (Fig. 4G). The reasons why the Raman signal is decreasing are as follows. The 3′ part of the aptamer strand is close to the SNF surface before the SARS-CoV-2 S protein binds. After binding, a 3D structure consisting of an aptamer-protein complex is formed, which is expected to decrease the Raman signal as the 3′ part of the aptamer moves away from the SNF surface. These results confirmed that the SNF substrate can be used as an effective SERS substrate and that this aptasensor is the most sensitive for the detection of the SARS-CoV-2 S protein when we employ our best aptamer (Fig. 4G and Table S2).

3.4. Clinical validation of our SERS aptasensor for multiple SARS-CoV-2 variants

Since the initial discovery of SARS-CoV-2 in 2019, the ancestral Wuhan wild-type strain has given rise to a host of variants with altered transmissibility, pathogenicity, and potential for immune escape, including the Alpha (B.1.1.7), Beta (B.1.351), Gamma (P.1), Epsilon (B.1.429), Delta (B.1.617.2), and Omicron (B.1.1.529) variants. Although various commercial RATs have been developed for these, several of these have proven incapable of detecting the now-widespread Omicron variant, even days after the infection (Adamson et al., 2022). This remains a serious problem for managing the spread of COVID-19, and given that this virus still has abundant opportunities for the

emergence of novel lineages, there is a clear need for diagnostic tools capable of detecting a broad range of variants.

We, therefore, validated the utility of our aptasensor platform using SpS1-C4 for testing actual clinical samples collected from patients with COVID-19 (Fig. 5 and Figs. S10–S13). Considering the improved accuracy, SpS1-C4 was chosen to validate clinical samples because it is 1000-fold more sensitive than the SpS1-C1 aptamer. We used 80 clinical nasopharyngeal samples obtained from the Sejong Institute of Health & Environment: 20 known negatives, and 20 samples each from known positives with wild-type, Delta, and Omicron variants. The results were verified by RT-qPCR (Table S3). In the negative samples, there was no binding with the target, and thus only a negligible difference in Raman signals at 1,587 cm^{-1}. In contrast, we consistently observed a dramatic decrease in Raman signals with all 60 COVID-19 positive samples (Fig. 5A–D and Figs. S10–S13). Using these data, we conducted a receiver operating characteristic (ROC) curve analysis to assess the sensitivity and specificity of the platform. Based on ROC analysis, we determined the decision threshold to be an intensity ratio of 0.5575 (Fig. 5E). The decision threshold was determined as the average between the sum of negative values and the sum of positive values of Wild-type, Delta, and Omicron in Fig. 5E. Only one sample showed a false negative (WT-15), and this was subsequently attributed to failed conjugation of the aptamer onto the SNF substrate, based on the absence of intrinsic Raman signals from the aptamer. The area under the curve

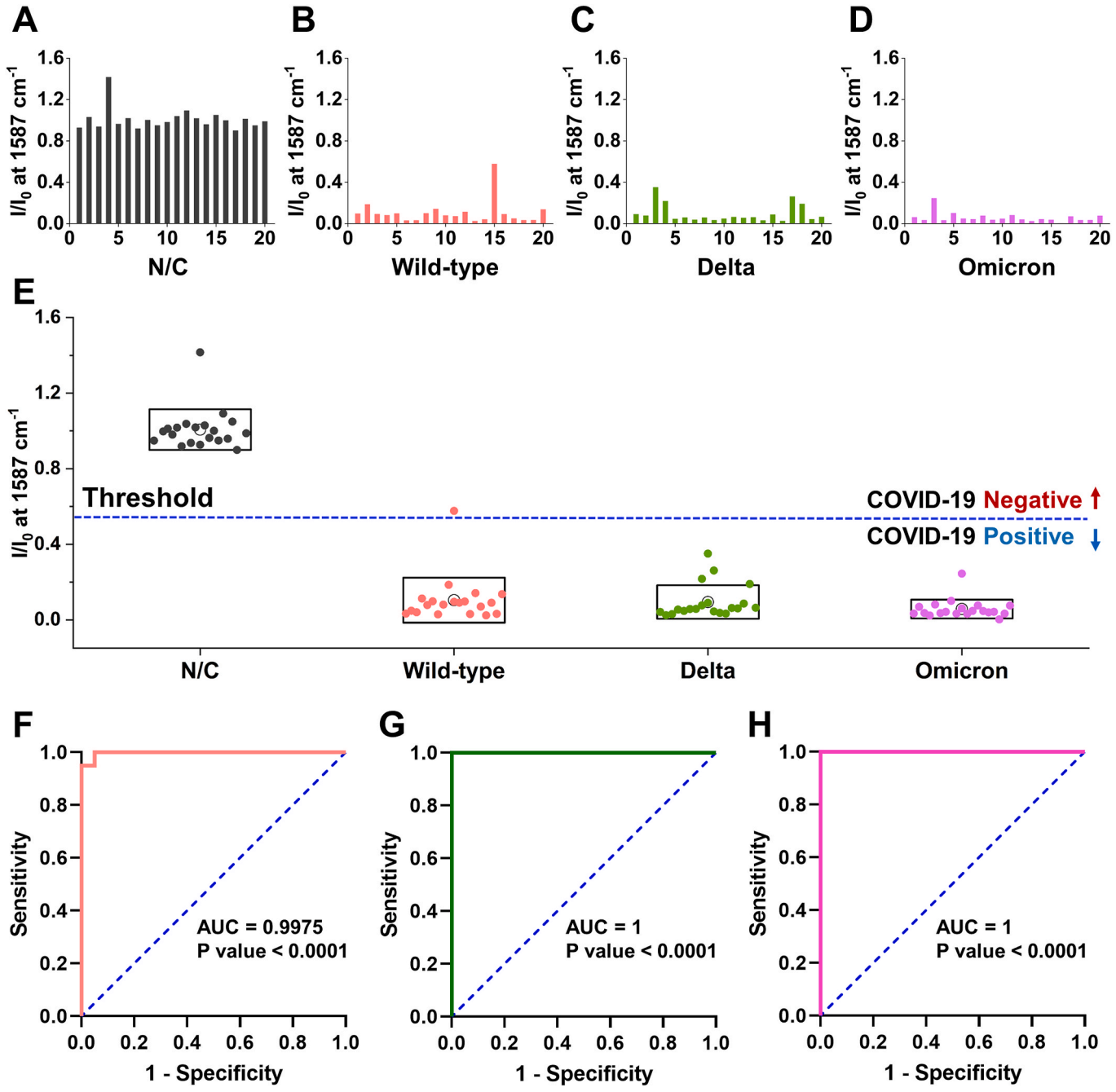

Fig. 5. Clinical validation of our SERS-based aptasensor. (A–D) SARS-CoV-2 detection in 80 nasopharyngeal specimens representing (A) negative controls or patients with (B) wild-type, (C) Delta, and (D) Omicron variants of SARS-CoV-2. (E) Sensitivity and specificity of detection of SARS-CoV-2 variants based on a threshold (dashed lines) calculated from the receiver operating characteristic (ROC) curve. The box indicates the standard deviation, and the white circle indicates the mean value. (F–H) ROC curves of diagnosis for (F) wild-type, (G) Delta, and (H) Omicron variants of SARS-CoV-2.

(AUC) was determined to be 0.9975, 1, and 1 for the WT, Delta, and Omicron variants, respectively, confirming the excellent accuracy for broad detection of SARS-CoV-2 (Fig. 5F–H).

Even though our aptamers were derived from an S protein from an early lineage of SARS-CoV-2 in 2020 (NCBI Reference Sequence: YP_009724390.1) (Wu et al., 2020), SpS1-C4 showed robust binding to the highly-mutated Delta and Omicron variants as well. Our aptamers bind to S1, which in turn recognizes the host-cell ACE2 receptor, and the results here indicate that this binding site may be especially well conserved across SARS-CoV-2 variants. Further studies will be required to clarify this, but our current results indicate that our platform could prove broadly applicable for detecting future variants of concern as well.

4. Conclusions

Timely diagnosis of SARS-CoV-2 is crucial to prevent the spread of the virus, particularly given the potential for emergence of new variants of concern that may elude existing diagnostic assays. Here, we report a label-free SERS-based aptasensor platform that combines a novel aptamer and silver nanoforest substrate to achieve ultra-sensitive, highly accurate detection of multiple SARS-CoV-2 variants. Using the particle display technique, we successfully isolated two DNA aptamers that exhibited a low nanomolar Kd for the viral S protein—to the best of our knowledge, this represents the highest-affinity aptamer reported to date for this target. We subsequently incorporated these aptamers into our label-free SERS-based aptasensor platform, achieving an attomolar detection limit for recombinant S protein. We then clinically validated our aptasensor platform with 60 clinical samples with SARS-CoV-2 (wild-type, Delta, and Omicron) and 20 negative controls, achieving excellent accuracy with high sensitivity and specificity for broad detection of SARS-CoV-2. This aptasensor has the potential to detect future variants of this virus, and the same design could be exploited to achieve rapid and economical development of diagnostic tools for a diverse range of other pathogens as well.

CRediT authorship contribution statement

Ki Sung Park: Conceptualization, Data curation, Formal analysis, Investigation, Writing – original draft. **Anna Choi:** Formal analysis, Investigation. **Hyun Jung Kim:** Formal analysis, Investigation. **Insu Park:** Formal analysis, Investigation. **Mi-Suk Eom:** Resources, SARS-CoV-2 clinical samples. **Sang-Gu Yeo:** Resources, SARS-CoV-2 clinical samples. **Ryeo Gang Son:** Formal analysis, Investigation. **Tae-In Park:** Formal analysis, Investigation. **Gyudo Lee:** Formal analysis, Investigation. **Hyongsok Tom Soh:** Conceptualization, Writing – review & editing. **Yoochan Hong:** Project administration, Data curation, Formal analysis, Writing – review & editing. **Seung Pil Pack:** Project administration, Data curation, Formal analysis, Writing – review & editing, All the authors discussed and approved the manuscript.

Declaration of competing interest

The authors declare that they have no known competing financial interests or personal relationships that could have appeared to influence the work reported in this paper.

Data availability

Data will be made available on request.

Acknowledgments

This work was supported by the National Research Foundation of Korea (NRF) funded by the Korean government (MSIT) (NRF-2021R1A5A8032895, NRF-2021R1A2C2011564). This work was also supported by Korea Institute of Machinery & Materials (KIMM) (NK244D). This work was supported by ReGenesys Lab Co. Ltd. This work was also supported by Korea University.

Appendix A. Supplementary data

Supplementary data to this article can be found online at https://doi.org/10.1016/j.bios.2023.115202.

References

Abdelhamid, M.A., Son, R.G., Park, K.S., Pack, S.P., 2022. Colloids Surf., B 219, 112830.
Adamson, B., Sikka, R., Wyllie, A., Premsrirut, P., 2022. Medrxiv 5. Preprint posted online, 2022-01. https://doi.org/10.1101/2022.01.04.22268770.
Ahmad, K.M., Oh, S.S., Kim, S., McClellen, F.M., Xiao, Y., Soh, H.T., 2011. PLoS One 6 (11), e27051.
Ambartsumyan, O., Gribanyov, D., Kukushkin, V., Kopylov, A., Zavyalova, E., 2020. Int. J. Mol. Sci. 21 (9), 3373.
Banerji, A., Wickner, P.G., Saff, R., Stone Jr., C.A., Robinson, L.B., Long, A.A., Wolfson, A.R., Williams, P., Khan, D.A., Phillips, E., 2021. J. Allergy Clin. Immunol. Pract. 9 (4), 1423–1437.
Barhoumi, A., Halas, N.J., 2010. J. Am. Chem. Soc. 132 (37), 12792–12793.
Broughton, J.P., Deng, X., Yu, G., Fasching, C.L., Singh, J., Streithorst, J., Granados, A., Sotomayor-Gonzalez, A., Zorn, K., Gopez, A., 2020. Nature biotechnology 38 (7), 870–874. MedRxiv. https://doi.org/10.1038/s41587-020-0513-4.
Chen, A., Yang, S., 2015. Biosens. Bioelectron. 71, 230–242.
Corman, V.M., Landt, O., Kaiser, M., Molenkamp, R., Meijer, A., Chu, D.K., Bleicker, T., Brünink, S., Schneider, J., Schmidt, M.L., 2020. Euro Surveill. 25 (3), 2000045.
Diehl, F., Li, M., He, Y., Kinzler, K.W., Vogelstein, B., Dressman, D., 2006. Nat. Methods 3 (7), 551–559.
Dressman, D., Yan, H., Traverso, G., Kinzler, K.W., Vogelstein, B., 2003. Proc. Natl. Acad. Sci. U.S.A. 100 (15), 8817–8822.
Drolet, D.W., Moon-McDermott, L., Romig, T.S., 1996. Nat. Biotechnol. 14 (8), 1021–1025.
Ellington, A.D., Szostak, J.W., 1990. Nature 346 (6287), 818–822.
Emery, S.L., Erdman, D.D., Bowen, M.D., Newton, B.R., Winchell, J.M., Meyer, R.F., Tong, S., Cook, B.T., Holloway, B.P., McCaustland, K.A., 2004. Emerg. Infect. Dis. 10 (2), 311.
Gans, J.S., Goldfarb, A., Agrawal, A.K., Sennik, S., Stein, J., Rosella, L., 2022. JAMA 327 (5), 485–486.
Gao, W., Li, B., Yao, R., Li, Z., Wang, X., Dong, X., Qu, H., Li, Q., Li, N., Chi, H., 2017. Anal. Chem. 89 (18), 9836–9842.
Gillibert, R., Triba, M.N., de la Chapelle, M.L., 2018. Analyst 143 (1), 339–345.
Hsieh, C.-L., Goldsmith, J.A., Schaub, J.M., DiVenere, A.M., Kuo, H.-C., Javanmardi, K., Le, K.C., Wrapp, D., Lee, A.G., Liu, Y., 2020. Science 369 (6510), 1501–1505.
Hu, P., Zhu, C., Jin, L., Dong, S., 2012. Biosens. Bioelectron. 34 (1), 83–87.
Hwang, M.T., Park, I., Heiranian, M., Taqieddin, A., You, S., Faramarzi, V., Pak, A.A., van der Zande, A.M., Aluru, N.R., Bashir, R., 2021. Adv. Mater. Technol. 6 (11), 2100712.
Jayasena, S.D., 1999. Clin. Chem. 45 (9), 1628–1650.
Kellner, M.J., Koob, J.G., Gootenberg, J.S., Abudayyeh, O.O., Zhang, F., 2019. Nat. Protoc. 14 (10), 2986–3012.
Kim, H.S., Lee, T., Yun, J., Lee, G., Hong, Y., 2021. Microchem. J. 160, 105632.
Li, Z., Yi, Y., Luo, X., Xiong, N., Liu, Y., Li, S., Sun, R., Wang, Y., Hu, B., Chen, W., 2020. J. Med. Virol. 92 (9), 1518–1524.
Moskovits, M., 1985. Rev. Mod. Phys. 57 (3), 783.
Pang, S., Labuza, T.P., He, L., 2014. Analyst 139 (8), 1895–1901.
Park, I., Lim, J., You, S., Hwang, M.T., Kwon, J., Koprowski, K., Kim, S., Heredia, J., Stewart de Ramirez, S.A., Valera, E., 2021. ACS Sens. 6 (12), 4461–4470.
Podder, S., Ghosh, A., Ghosh, T., 2021. J. Med. Virol. 93 (5), 2790–2798.
Scatena, E., Baiguera, S., Del Gaudio, C., 2019. Journal of Healthcare Engineering 2019, 2815789, 2019, 11 pages. https://doi.org/10.1155/2019/2815789.
Shao, K., Ding, W., Wang, F., Li, H., Ma, D., Wang, H., 2011. PLoS One 6 (9), e24910.
Simpson, S., Kaufmann, M.C., Glozman, V., Chakrabarti, A., 2020. Lancet Infect. Dis. 20 (5), e108–e115.
Spinelli, A., Pellino, G., 2020. Br. J. Surg. 107 (7), 785–787.
Taghdisi, S.M., Danesh, N.M., Beheshti, H.R., Ramezani, M., Abnous, K., 2016. Nanoscale 8 (6), 3439–3446.
Wang, J., Gong, Q., Maheshwari, N., Eisenstein, M., Arcila, M.L., Kosik, K.S., Soh, H.T., 2014. Angew. Chem. Int. Ed. 126 (19), 4896–4901.
Wu, F., Zhao, S., Yu, B., Chen, Y.-M., Wang, W., Song, Z.-G., Hu, Y., Tao, Z.-W., Tian, J.-H., Pei, Y.-Y., 2020. Nature 579 (7798), 265–269.
Yang, G., Li, Z., Mohammed, I., Zhao, L., Wei, W., Xiao, H., Guo, W., Zhao, Y., Qu, F., Huang, Y., 2021. Signal Transduct. Targeted Ther. 6 (1), 227.
Zhao, J., Pinchuk, A.O., McMahon, J.M., Li, S., Ausman, L.K., Atkinson, A.L., Schatz, G. C., 2008. Acc. Chem. Res. 41 (12), 1710–1720.
Zhou, J., Rossi, J., 2017. Nat. Rev. Drug Discov. 16 (3), 181–202.